Chapter 4

EXAFS Study on Yttrium oxide thin films

In Chapter 3 the effect of variation of self bias on the structure and properties of the deposited yttrium oxide thin films is discussed. The changes occurring due to variation of bias on the substrates could be estimated from the results of various characterization techniques. To gain further insight and understand the changes in local structure with the substrate bias, EXAFS measurements are carried out on these thin films. AFM measurements are also done to study morphology of the deposited films. Information regarding co-ordination number, bond length and disorder parameter obtained from EXAFS analysis is correlated with properties of films obtained by other characterization techniques

4.1 Introduction

EXAFS deals with the measurement of fine structures in the X-ray absorption spectra above the absorption edge of the atoms in a material. The fine oscillatory structure in the X-ray absorption spectra of a particular species of atom gives precise information regarding the radial arrangement of atoms around that element and with the advent of modern bright synchrotron radiation sources, this technique has emerged out to be most powerful for local structure determination which can be applied to any type of material viz. amorphous, polycrystalline, polymers, surfaces and solutions [**97**].

EXAFS studies on Y_2O_3 thin films have been reported earlier by different groups. Unlike XRD technique, EXAFS does not require samples with long range structural order and hence this technique is used for study of nanocrystalline samples [**112, 113**]. In case of EXAFS study on nanocrystalline Y_2O_3, presence of Y-(OH) at the particle surface was

reported [**112**]. Nano-Y_2O_3 and nano-ZrO_2 ceramics were investigated by EXAFS and it was found that the cation- oxygen co-ordination is higher in sintered nano-ceramics as compared to powders of micrometer size. It was reported that after sintering, the disorder in cation-oxygen co-ordination of nano ceramics decreases compared to powders of micrometer size [**113**]. Cheng Xue-Rui et al. have observed that Y-O bond length and co-ordination number decrease below six due to the presence of oxygen vacancies in Y_2O_3 films [**114**]. They have concluded that presence of oxygen vacancy would change the electron band structure affecting the physical properties of the films. The effect of adsorption of water on Y_2O_3 was studied with EXAFS by Kuroda et al. and it was found that three types of reactions of water with Y_2O_3 are possible [**115**]. It was reported that water was physisorbed, can be strongly adsorbed and can further react to form YO-OH type of bonds. EXAFS study of Y_2O_3 thin films deposited by RF plasma enhanced MOCVD and correlation of local structure of Y_2O_3 with variation of bias voltage has not been reported earlier.

4.2 Experimental details for EXAFS measurement

EXAFS measurements on these samples at Y K edge are carried out in fluorescence mode at the Scanning EXAFS Beamline (BL-9) at the INDUS-2 Synchrotron Source (2.5 GeV, 100 mA) at the Raja Ramanna Centre for Advanced Technology (RRCAT), Indore, India. The schematic of experimental set-up for EXAFS measurement is given in **Figure 4.1**. The beamline uses a double crystal monochromator (DCM) which works in the photon energy range of 4-25 KeV with a resolution of 10^4 at 10 KeV. A 1.5 m horizontal pre-mirror with meridonial cylindrical curvature is used prior to the DCM for collimation of the beam and higher harmonic rejection. The second crystal of the DCM is a saggital cylinder with

radius of curvature in the range 1.28-12.91 meter which provides horizontal focusing to the beam. For measurements in the fluorescence mode, the sample is placed at 45° to the incident X-ray beam and the fluorescence signal (I_f) is detected using a Si drift detector placed at 90° to the incident X-ray beam. An ionization chamber is used prior to the sample to measure the incident X ray flux (I_0) and the absorbance of the sample ($\mu = \frac{I_f}{I_0}$) is obtained as a function of energy by scanning the monochromator over the specified energy range. The absorption spectra of the samples at Y K edge are recorded in the energy range 16960- 17650 eV.

AFM measurements are carried out on Y_2O_3 thin films in semi-contact mode using NT-MDT make P47H SPM system with a diamond like carbon tip having radius of curvature 1-3 nm.

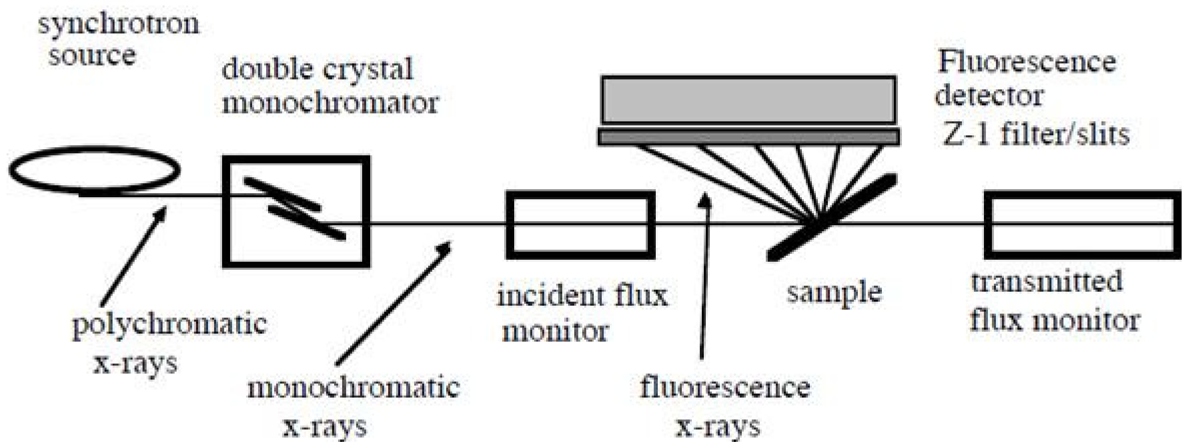

Figure 4.1: Schematic of experimental EXAFS set-up [Ref-**116**]

4. 3 Characterization results

4.3.1 *Extended X-ray Absorption fine spectroscopy*

Figure 4.2 shows the stacked raw EXAFS (normalized (μ) versus E) spectra of the various Y_2O_3 films deposited on silicon substrate under different substrate bias conditions. In order to take care of the oscillations in the absorption spectra, the energy dependent absorption coefficient $\mu(E)$ has been converted to absorption function $\chi(E)$ defined as follows:

$$\chi(E) = \frac{\mu(E) - \mu_0(E)}{\Delta\mu_0(E_0)} \qquad (4.1)$$

where E_0 absorption edge energy, $\mu_0(E_0)$ is the bare atom background and $\Delta\mu_0(E_0)$ is the step in the $\mu(E)$ value at the absorption edge. After converting the energy scale to the photoelectron wave number scale (k) as defined by,

$$k = \sqrt{\frac{2m(E - E_0)}{\hbar^2}} \qquad (4.2)$$

the energy dependent absorption coefficient $\chi(E)$ has been converted to the wave number dependent absorption coefficient $\chi(k)$, where m is the electron mass. The $k\chi(k)$ versus k spectra derived from the μ versus E spectra have been shown in **Figure 4.3** for all the samples. The analyzable k range of the data is from 3-10 $Å^{-1}$ and the $\chi(k)$ spectra is weighted by k to amplify the oscillations at high k .

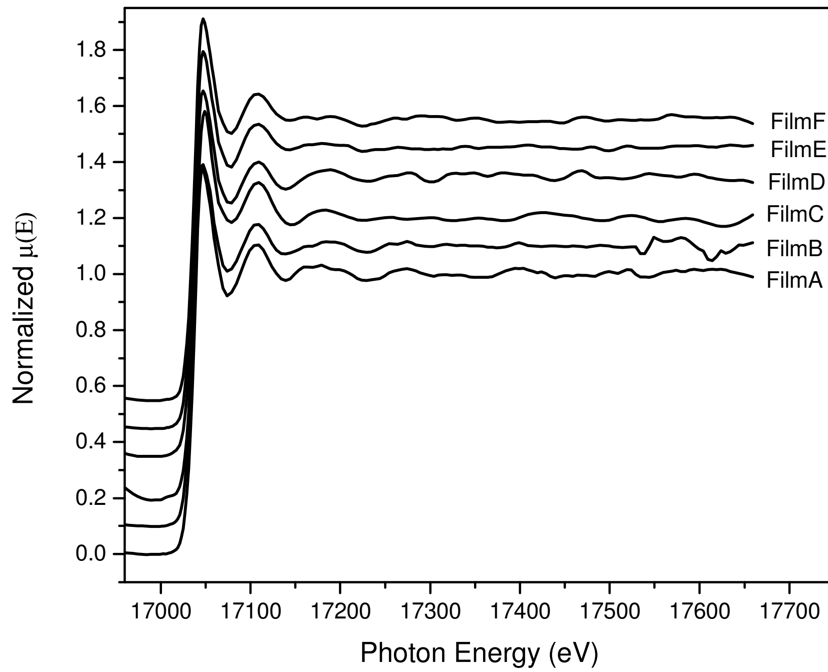

Figure 4.2: EXAFS spectra of Y_2O_3 films deposited at different bias voltage levels

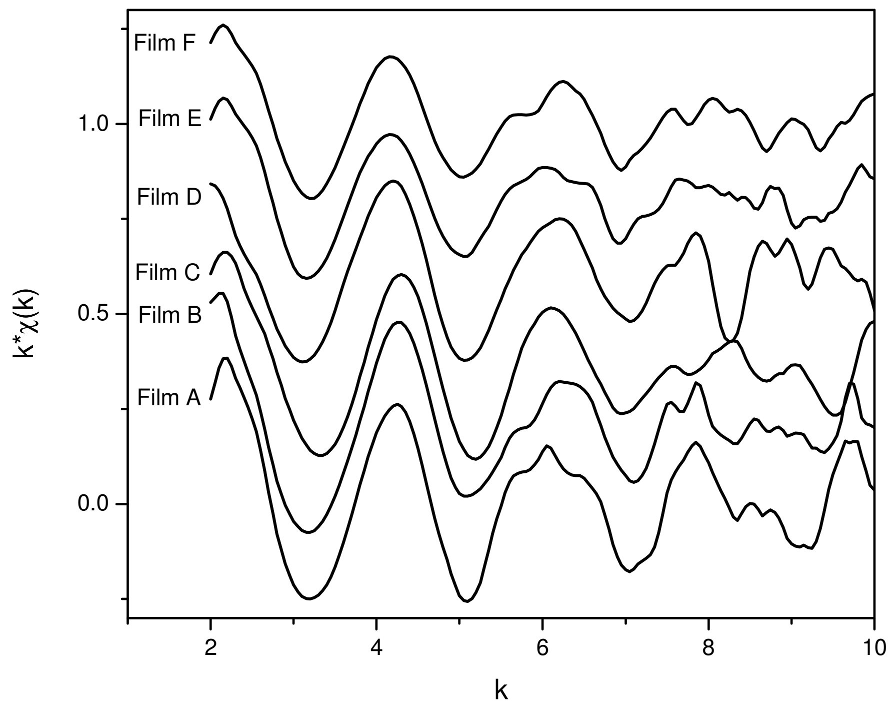

Figure 4.3: $k\,\chi(k)$ versus k spectra of Y_2O_3 films deposited at different bias voltage levels

A set of EXAFS data analysis program available within the IFEFFIT software package [**117**] have been used for reduction and fitting of the experimental EXAFS data. This includes data reduction and Fourier transform to derive the $\chi(r)$ versus r spectra from the $k\chi(k)$ versus k spectra, generation of the theoretical EXAFS spectra starting from an assumed crystallographic structure and finally fitting of the experimental data with the theoretical spectra using the FEFF 6.0 code. The goodness of the fit in each case is decided by the lowest attainable value of the parameter R which is defined as [**118**]:

$$R = \sum \frac{[\mathrm{Im}(\chi_{dat}(r_i) - \chi_{th}(r_i)]^2 + [\mathrm{Re}(\chi_{dat}(r_i) - \chi_{th}(r_i)]^2}{[\mathrm{Im}(\chi_{dat}(r_i)]^2 + [\mathrm{Re}(\chi_{dat}(r_i)]^2} \qquad (4.3)$$

Where, χ_{dat} and χ_{th} refer to the experimental and theoretical $\chi(r)$ values respectively and Im and Re refer to the imaginary and real parts of the respective quantities.

The experimental $\chi(r)$ versus r FT-EXAFS spectra of the Y_2O_3 thin film samples at Y K edge have been fitted with theoretical spectra assuming bixbyite structure with space group Ia3. The bixbyite structure is a body centered cubic structure in which the Y cation occupies two inequivalent sites i.e. the 8 C_{3i} and 24 C_2 positions. However the Y-O bond distances for the two Y sites are very close. Hence, this structure has been fitted from 1.2 to 2.4 Å assuming an average Y-O shell at 2.27Å (×6). The structural parameters for the above mentioned structure are obtained from the reported values in the literature [**52**]. **Figure 4.4** shows the experimental $\chi(r)$ versus r spectra of all the Y_2O_3 thin film samples deposited at different bias voltage along with the best fit theoretical plots carried out as above and the values of the parameter R for the best fit in each case have been given in the respective plots. Only the first co-ordination shell corresponding to Y-O bond is used for fitting. The bond distances (r), co-ordination numbers (N) (including scattering amplitudes) and disorder

(Debye-Waller) factors (σ^2), which give the mean-square fluctuations in the distances, have been used as fitting parameters. The EXAFS fitting results are tabulated in **Table 4.1**.

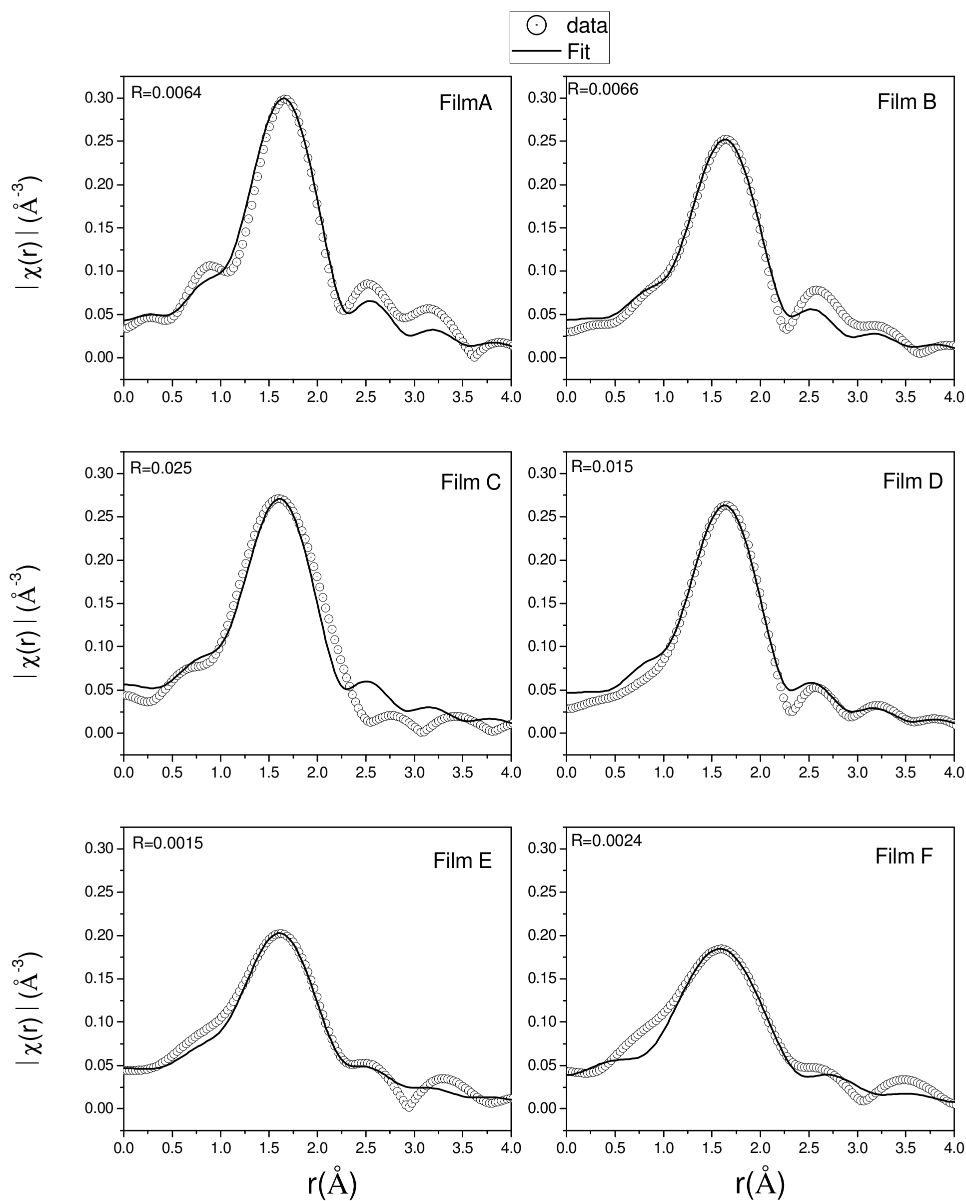

Figure 4.4: Experimental $\chi(r)$ versus r spectra along with best fit theoretical plots of Y_2O_3 films deposited at different bias voltage levels

	Film A	Film B	Film C	Film D	Film E	Film F
RF Self Bias (V)	-50	-75	-100	-125	-150	-175
Y-O Bond						
R(Å)	2.232±0.005	2.221±0.005	2.197±0.011	2.219±0.008	2.211±0.003	2.211±0.003
N	5.7±0.2	5.2±0.2	5.4±0.5	5.4±0.4	5.5±0.2	5.4±0.2
σ^2	0.0010±0.0009	0.0025±0.0009	0.0025±0.0019	0.0025±0.0013	0.0082±0.0005	0.0082±0.0008

Table 4.1: EXAFS Fitting Results

The variation of Y-O bond length, co-ordination number and disorder parameter with bias voltage is shown in **Figure 4.5** along with their respective uncertainties obtained from the fitting.

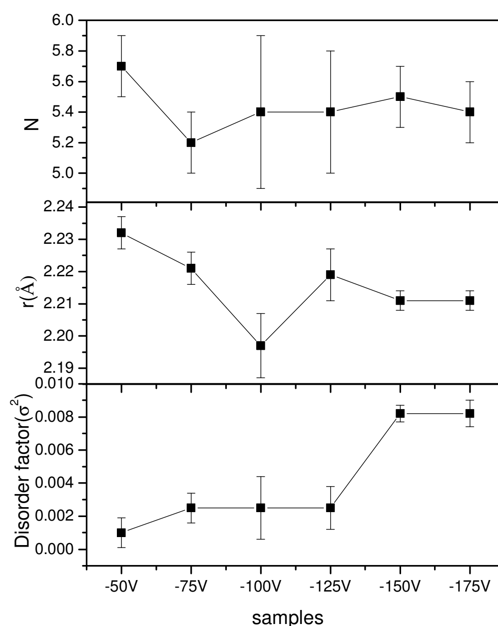

Figure 4.5: Variation of co-ordination number, bond length and Debye Waller factor with RF self-bias voltage

EXAFS analysis indicates that the local structure of the films changes with change in RF self- bias.

4.3.2 *Atomic Force Microscopy*

The 3D AFM images for the films A-F are shown in **Figure 6(a-f)** respectively and the results of AFM measurements are tabulated in **Table 4.2**.

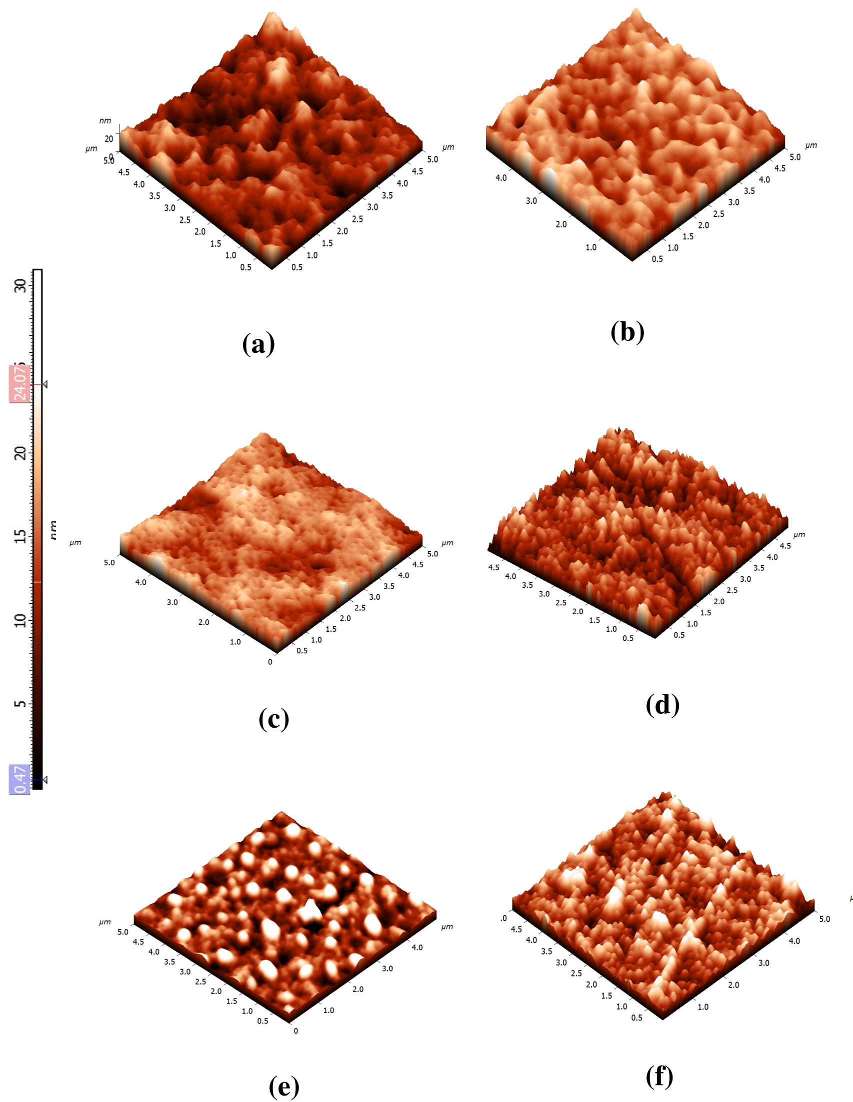

Figure 4.6 (a-f): 3D AFM images of Y_2O_3 films deposited at different bias levels

Film	Root mean square roughness (nm)	Entropy
A	4.3	8.6
B	3.1	8.2
C	4.0	8.5
D	12.3	10.1
E	8.8	9.4
F	15.5	10.4

Table 4.2: AFM analysis of films deposited at various bias voltages

The expressions used for calculating root mean square roughness (R_q) and entropy $(H(Z))$ values [**119**] are given below,

$$R_q = \sqrt{(1/N_x * N_y)\sum_{j=1}^{N_y}\sum_{i=1}^{N_x}(Z_{ij} - \mu)^2}$$

$$H(Z) = -\sum_{Z} p(Z)\log_2 p(Z)$$

where, $Z_{ij} = Z(X_i, Y_j)$ is a discrete function set on XY plane, N_x and N_y are number of points on X and Y axes, μ is the average height and $p(Z)$ is the discrete probability distribution of one dimensional random variable.

The surface morphology of deposited films is also found to change with self bias. It is observed that the root mean square roughness and entropy values increase for films deposited at bias voltages higher than -100 V.

4.4 Discussion: Effect of bias variation on local structure of Y_2O_3

Our earlier analysis given in chapter-3 from the GIXRD patterns shown in **Figure 3.3** indicates that films A-D have polycrystalline BCC yttrium oxide structure while there is broadening of GIXRD peaks in case of films E and F. It is observed that film A has no preferred orientation; while films B and D show preferred growth along (111) direction and film C shows (100) as preferred growth direction. However, IR spectra reported earlier [**Figure 3.6**] indicate that all films have cubic Y_2O_3 structure.

The co-ordination number and bond length for bulk Y_2O_3 are 6 and 2.27Å respectively [**52**]. However from EXAFS analysis shown in **Figure 4.5**, it can be seen that in case of thin films, the co-ordination number and bond length are smaller as compared to the bulk. This may be due to small degree of non-stoichiometry in the deposited phase present on the surface of the films as reported earlier [**120**]. Dangling unsaturated bonds on surface of the thin films can result in decrease in bond length as well as reduction in co-ordination number.

As seen from **Figure 4.5**, the oxygen co-ordination is high for film A as compared to film B. Earlier XPS analysis (given in **Table 3.3**) indicates significantly high presence of hydroxyl and carbonate group in film A. This is supported by AFM measurements which show presence of valleys on the surface of film A.

At low bias level the decomposition of precursors is not efficient. The energy of ions impinging on the substrate is less resulting in formation of voids. These voids act as favorable sites for moisture adsorption [**51**] and hence oxygen co-ordination is high for film A [**115**]. In case of film B, with increase in bias level, the energy of ions increase, there is improvement in precursor fragmentation and ions impinge on the substrate with higher

energy. Hence there is reduction in void formation resulting in decrease in adsorption of hydroxyl group which finally leads to decrease in oxygen co-ordination as compared to film A. From **Figure 4.6(b)** also it is seen that the formation of valleys on the surface in case of film B has decreased as compared to film A resulting in more smoother films with lower r.m.s. roughness as shown in **Table-4.2**. As reported earlier [**120**] the thickness of film B is also higher (250 nm) as compared to film A (140 nm) which is due to the enhanced plasma activity at RF self-bias of -75 V as compared to -50 V bias. Surface energy minimization favors growth along (111) direction and thus this indicates that in case of film B the energy of ad atoms is sufficient for the growth to take place along (111) direction. The enhancement of density of film B as compared to film A can also be seen from the ellipsometry results discussed earlier [**Figure 3.1**], which shows that the refractive index of film B is higher as compared to refractive index of film A.

However, in case of film C, though **Figure 4.6(c)** shows that roughness is less compared to film A. The refractive index is also found to be less than that of film A as orientation of film C is in (100) direction which is not densely packed as (111) plane [**63**]. From XPS analysis (**Table 3.3**), it is seen that there is increase in degree of stoichiometric yttrium oxide in case of film C, indicating increased oxygen reactivity and hence increased co-ordination . This can lead to change in oxygen vacancy concentration resulting in change of orientation to (100) [**59**] and decrease in thickness (65 nm). From **Figure 3.1**, it can be seen that film D has higher refractive index compared to film C because of its preferred orientation in (111) direction. AFM 3D image for the film D (**Figure 4.6(d)**) shows more sharp features as compared to films deposited at lower bias voltages indicating higher roughness of film D. This corroborates with GIXRD pattern of film D which shows increased

FWHM of diffraction peak as compared to films deposited at lower bias voltages indicating decrease in domain size. This decrease in coherently scattering domain size indicates the onset of dominance of sputtering effect over ad atom organization. It can be observed from **Figure 4.4**, that the theoretical fitting of the FT-EXAFS i.e., $\chi(r)$ versus r data of the films C and D are not as good as that of the films A and B, showing higher values for the R parameter and higher uncertainties in the derived values of the fitting parameters as shown in **Figure 4.5**. This is possibly due to the change in the preferred crystallographic orientation in the film C which has affected its local structure around the Y atoms. Though the effect is more pronounced in case of film C affecting both its local and long-range order, in case film D, the effect remains significant in the local structure.

In case of films E and F, which are deposited at bias level beyond -125 V, re-sputtering mechanism further dominates over surface reorganization of ad atoms. This results in higher disorder in films leading to formation of nanocrystalline structure. This can be seen from the GIXRD measurements which show broadened diffraction peaks for these samples. There is also a progressive decrease in thickness of films E (108 nm) and F (75 nm) due to dominating effect of resputtering. From **Figure 3.1** it can be seen that film E has highest refractive index due to nanocrystalline nature as reported by Ramana et al. [**65**]. As can be seen from **Table 4.2** the r.m.s. roughness value for film E is less compared to film D due to the nanocrystalline nature of film E with relatively smaller grain size. **Figure 4.6(f)** however shows sharper features on the surface of film F indicating higher roughness value which may be due to increase in level of structural distortion due to significant bombardment in case of film F. Due to this reason film F also exhibits the minimum value of refractive index. It can be seen from **Figure 4.4** and **4.5** that the fitting quality of the $\chi(r)$ versus r data is better for

both the films E and F compared to the films C and D with lower values of the R parameter and lower uncertainties for the fitting parameters. This shows that the local structures around Y atom of these nanocrystalline samples are similar (viz., single oxygen shell in nearest neighborhood) to that of the polycrystalline sample deposited at lower bias voltages viz., the film B. However, nanostructures have increased surface area resulting in higher adsorption of atmospheric gases on the surface and hence there is a slight increase in oxygen co-ordination in case of films E and F compared to the film B as indicated by EXAFS analysis and shown in **Figure 4.5** [**111**].

As seen from **Figure 4.5**, the bond length in general decreases with bias. As bias increases there is reduction in void formation so the amount of adsorbed hydroxyl group decreases resulting in decrease in bond length. The Y-OH bond length is greater than Y-O bond length [**112, 113**]. However **Figure 4.5**, shows that there is abrupt decrease in bond length for film C as compared to films B and D. As has been observed from GIXRD measurements (**Figure 4.7**), the orientation of film C is along (100) direction whereas films B and D are oriented in (111) direction. So, the surface energy of film C is higher as compared to films B and D. The number of dangling bonds at the surface will increase. This leads to a compressive stress in film C, reducing the Y-O bond length as compared to films B and D [**121**] whereas it can be seen that films B and D (both oriented along (111) direction) show similar Y-O bond length. As has been discussed earlier, films E and F show broadened XRD peaks indicating formation of nanocrystalline structure. It is observed that the bond length is reduced for film E and F as compared to film D. Similar reduction of bond length with increasing structural distortion and enhancement of refractive index in case of HfO_2-SiO_2 thin films have also been earlier reported by Das et al. [**122**].

From **Figure 4.5**, it is observed that the Debye-Waller factor (σ^2) increases slightly for film B as compared to film A and remains same for films B-D. The Debye-Waller factor again increases significantly for the films E and F which implies poor crystallinity of these films which has also been observed from GIXRD measurements. Increase in disorder with decrease in particle size has been earlier reported by Zeming Qi et al. for nanocrystalline Y_2O_3: Eu powder particles [**123**]. The above mentioned results on Debye-Waller factor obtained from EXAFS measurements thus corroborate the results obtained earlier by GIXRD [**120**] that films deposited at -150 V and -175 V show nanocrystalline structure. This is due to enhanced sputtering at high bias voltages.

Conclusion

Local structure and surface morphology of Y_2O_3 thin films deposited by RF plasma-assisted MOCVD technique with different RF self-bias has been investigated by EXAFS and AFM technique. As RF self-bias increases the Y-O bond length reduces resulting in more stoichiomeric and denser coating. However, for films deposited beyond a certain bias level, the Debye-Waller factor significantly increases manifesting realization of nanostructured films with structural distortion. AFM measurements also indicate that surface morphology of the films changes with change in bias voltage, where it has been found that with initial increase in substrate bias more compact microstructure is realized with lower r.m.s. roughness. However, roughness increases significantly again as bias is increased beyond –100 V possibly due to dominating effect of re-sputtering. The changes observed in local structural parameters of the films as obtained above could well be correlated with the observed macroscopic properties of the films.